Chapter 5

Numerical Results

5.1 Results for Testing the Generalized TVD Algorithm

As discussed in section 3.2, we have developed a new numerical analysis technique for this research: A generalized TVD algorithm (Nutaro, Riyavong and Ruffolo, 2000). To ensure that our new method is applicable to general advection type problems, we performed test simulations of the transport of charged particles under the influence of an Archimedean magnetic field. These particles undergo several physical process (see more details in Ruffolo 1995). Next, the performance of the numerical algorithm for the "planar shock" case has been tested. The results of these two case studies are known and well-established.

5.1.1 Without a shock

Before considering an oblique shock, we tested our methodology by reproducing the results of previous work. In a previous comparison with other codes (Earl *et al.*, 1995), we found that a particularly strenuous test is whether the code properly treats processes at early times, i.e., $t \ll \tau$, the mean free time. Therefore, we sought to reproduce previous results on the formation of coherent pulses of solar cosmic rays after an instantaneous injection at a starting point $z = 0$, defined to be 0.01 astronomical units (AU) from the Sun (Ruffolo and Khumlumlert, 1995).

We started with the original z-grid spacing, and then enlarged Δz to improve the program running speed, and tested how much Δz could be increased without seriously affecting the accuracy of the code. We considered the distribution of protons of kinetic energy 46.8 MeV, corresponding to a momentum of 300 MeV c^{-1}, where c is the speed of light. Figure (5.1) shows the mean pitch angle cosine $\langle\mu\rangle$ plotted vs. the distance traveled vt. To compare with the previous results (solid line), we started with $\Delta z_0 = \Delta\mu v\Delta t = 1.6 \times 10^{-5}$ AU as in the previous work ($\circ$ symbols), where simulation is over $z = 0$ to 0.05 AU. We then exploited the advantages of the TVD method by enlarging Δz to 10 times ($+$ symbols) and 100 times larger ($\times$ symbols), while keeping $\Delta\mu$ the same. We found that when $\Delta z = \Delta z_0$, we obtain almost exactly the same results as previously. The results were slightly different when the grid size was enlarged, which we believe to be caused by the strong focusing effect close to the Sun.

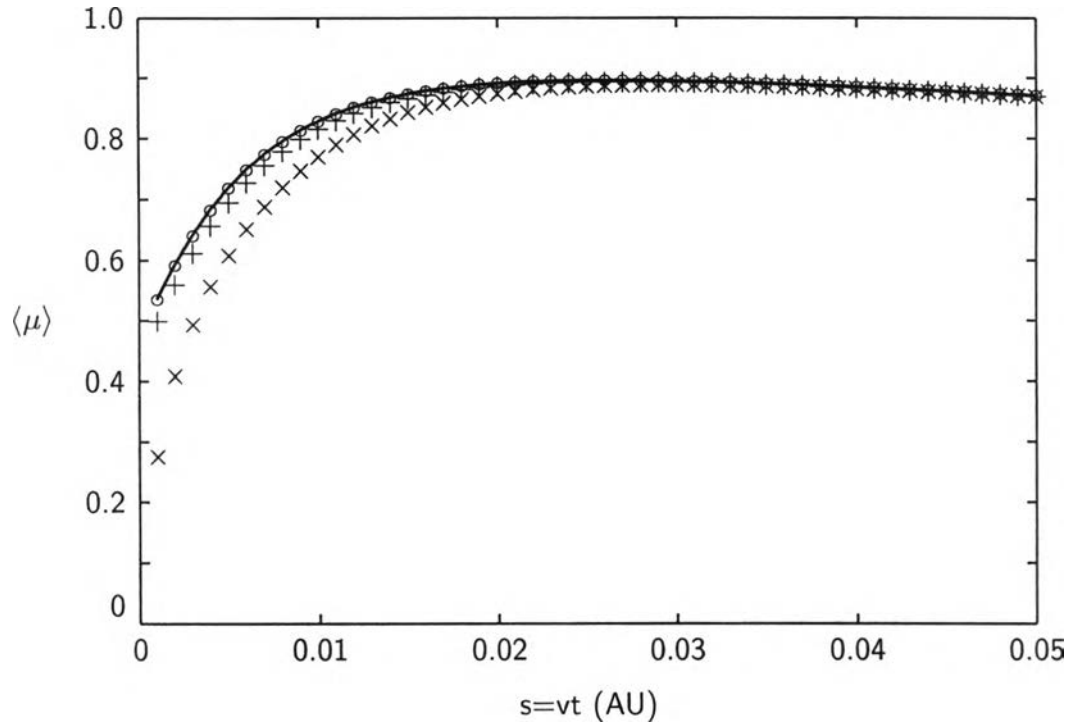

Figure 5.1: Comparison of the evolution of the mean pitch angle cosine $\langle\mu\rangle$ for a coherent pulse of solar cosmic rays up to $vt = 0.05$ AU for $\lambda = 0.3$ AU and $q = 1.5$ from Ruffolo and Khumlumlert (1995) with $\Delta z = 1.6 \times 10^{-5}$ (solid line) and by the generalized TVD method with $\Delta z = 1.6 \times 10^{-5}$ AU (o), 1.6×10^{-4} AU (+), and 1.6×10^{-3} AU (×).

The results all converge at around 0.02 AU, which is very small for practical purposes, given the approximations in the model, and that to date all measurements of solar cosmic rays have been at $\geq$ 0.3 AU from the Sun, while the calculation speed is commensurately improved by 1 or 2 orders of magnitude for the increased Δz values. Therefore, unless very high accuracy is required at such small radii, we conclude that this generalized TVD method can provide acceptable results while reducing the run time by 1 to 2 orders of magnitude.

The results of particle transport from the Sun to Earth orbit (a radius of 1 AU) were also examined. We set the simulation distance to be from $z = 0$ to 4 AU for $\Delta\mu = 2/25$ and with other values as before. Figure (5.2) illustrates the pitch angle-averaged F at Earth orbit vs. the distance traveled, $s = vt$. The results from previous work ($\Delta z_0 = \Delta\mu v\Delta t = 0.0016$) are indicated by solid lines, and our new results with the TVD method for Δz_0 are indistinguishable at this scale. Results are also shown for enlarged grid spacings 10 and 20 times bigger (dashed and dotted lines, respectively) while $\Delta\mu$ is the same. From Figure (5.2) we see that the pitch angle-averaged F obtained for $\Delta z = 10\Delta z_0$ is very similar to that in previous work, with the exception of a slight offset at late times (which when fitting observed data, would only affect the normalization). For $\Delta z = 20\Delta z_0$, we see evidence of numerical diffusion leading to an early arrival of particles for the highest grid spacing, though at a level $\sim 10^{-3}$ of the peak flux. Thus we conclude that $\Delta z = 10\Delta z_0$ provides good accuracy, and gives us a factor of 10 improvement in run speed.

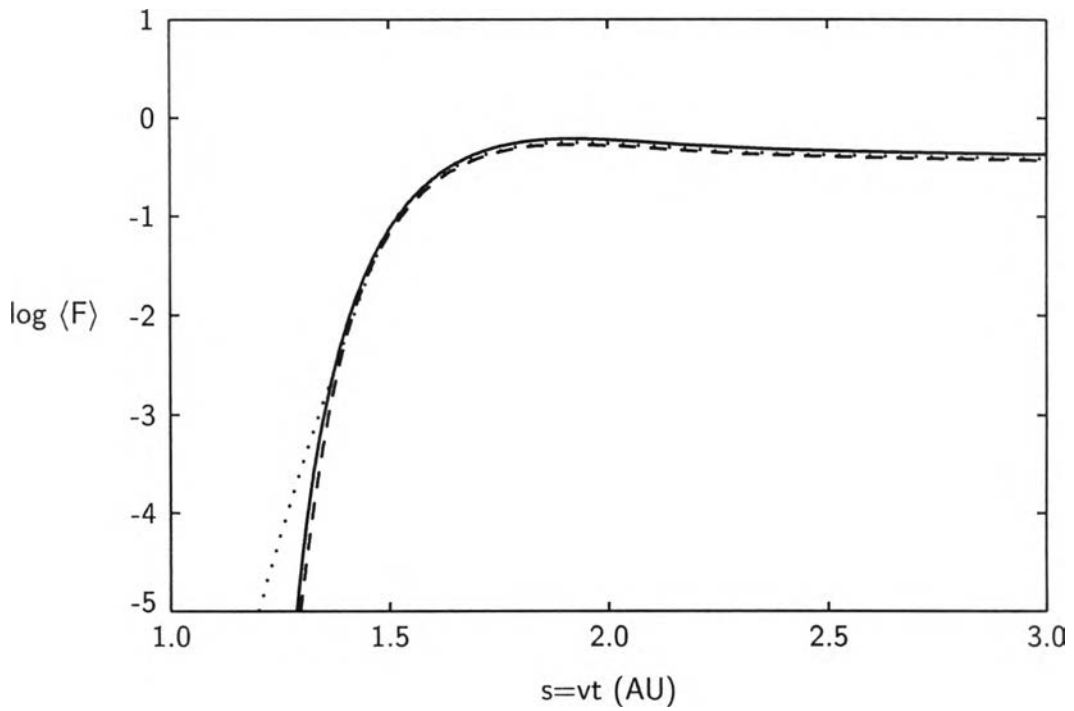

Figure 5.2: Pitch angle-averaged density of solar cosmic rays at Earth orbit. The simulation region is from 0 to 4 AU and $\Delta z = 0.016$ (dashed line) and 0.032 AU (dotted line). The results from Ruffolo and Khumlumlert(1995) ($\Delta z = 0.0016$) are indicated by the solid line.

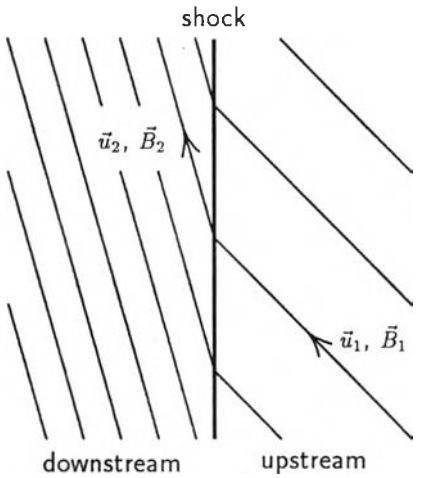

Figure 5.3: Schematic depiction of the background fluid motion near an oblique, planar, magnetohydrodynamic shock in the de Hoffmann-Teller frame. The shock is stationary and the flow speed is u_1 (upstream) or u_2 (downstream) along the magnetic field $\vec{B}_1$ or $\vec{B}_2$, respectively.

Finally, we note that this value of Δz is still less than $|v_z \Delta t|$ for the highest $|\mu|$ values, so $|\gamma| > 1$, and our generalization of the TVD method is necessary in order to obtain the level of accuracy that we require.

5.1.2 With an Oblique, Planar Shock

The distribution of particles encountering an oblique, planar shock (which for our purposes is a pre-existing discontinuity in the fluid speed background) was investigated using the new code. For more details of astrophysical implications, and the underlying theory, the reader is referred to Ruffolo (1999).

The results for steady state shock acceleration can serve to test the numerical code. For this special case, since $\partial F/\partial t = 0$, and we consider an ideal, plane-parallel shock with straight magnetic field lines on either side (Figure (5.3)), equation (1) in Ruffolo (1999) is substantially simplified, and separable solutions for $F(\mu, z)$ on one side of the shock can be found by solving an eigenvalue equation for μ. Therefore the resulting $F(\mu, z)$ on either the upstream or downstream side of the shock must be in the following form:

$$F(\mu,z) = \begin{cases} \displaystyle\sum_{n=0}^{\infty} \frac{a_n M_n(\mu)}{1-\mu uv/c^2} e^{k_n z} & (z>0, \text{ upstream}) \\ \displaystyle\sum_{n=-\infty}^{0} \frac{b_n M_n(\mu)}{1-\mu uv/c^2} e^{k_n z} & (z<0, \text{ downstream}), \end{cases}$$

where the $M_n(\mu)$ are eigenfunctions, a_n and b_n are coefficients and $k_n = \alpha_n A/(2v)$ for eigenvalues α_n (Ruffolo, 1999; Kirk and Schneider, 1987); for $u < 0$ (flow from upstream) these are such that $k_0 = 0$, $k_n < 0$ for $n > 0$, and $k_n > 0$ for $n < 0$. In addition to the boundary conditions at $z = \pm\infty$, there is a complicated boundary condition at the shock ($z = 0$) relating $F(\mu)$ immediately upstream and downstream (see §2 in Ruffolo (1999)). Therefore a numerical solution is required to evaluate the coefficients a_n and b_n. This numerical code was the first to solve this fundamental problem for mildly relativistic particles. In addition, modeling the shock acceleration of particles in the steady state serves as a test of the code, because the numerical method (which makes no reference to the eigenfunctions or eigenvalues) should yield a solution consistent with a linear combination of these

specific separable solutions. Figure (5.4) shows the steady state solution for the dependence of f on μ and z within $\pm 0.8\lambda$ of the shock, and Figure (5.5) shows the cross-section of f as function of μ for $z = \pm 0.05\lambda$. The parameters used (1 referring to upstream and 2 to downstream) were $q = 1$ and 1.5, $\tan\theta_1 = 4$ ($\theta_1 = 75°$), $\tan\theta_2 = 15.11$ ($\theta_2 = 86°$), u_1 (along $\vec{B}$)= 2244 km/s, $u_2 = 2185$ km/s, $v = 0.5c$, $F \propto p^{-\delta}$ with $\delta = 1.956$, $\Delta z/\lambda = 0.025$, $\Delta t = \Delta z/v$, and $\Delta\mu = 2/95$. For these parameters and $q = 1$, we have $\lambda = v/A$ [from equations (2) and (5)], and the eigenvalues correspond to length scales of $1/k_0 = \infty$, $1/k_1 = D/u = -22.25\lambda$ (upstream), $1/k_{-1} = 0.14\lambda$ (downstream), $1/k_2 = -0.13\lambda$ (upstream), $1/k_{-2} = 0.049\lambda$ (downstream), $1/k_3 = -0.046\lambda$ (upstream), and successively shorter length scales. In accordance with the permitted length scales, Figure (5.4) clearly shows that far from the shock, f is nearly constant downstream, and upstream is given by a constant plus a weakly anisotropic term that varies as $e^{uz/D}$ (with $u < 0$). These large scale features agree with those expected in the diffusion approximation (Ruffolo, 1999). One can also see deviations closer to the shock, and the numerical results are quantitatively consistent with a superposition of solutions of length scales $1/k_0$, $1/k_1$, $1/k_2$, and $1/k_3$ (upstream) and $1/k_0$, $1/k_{-1}$, and $1/k_{-2}$ (downstream); other eigenvalues correspond to length scales too fine to be resolved in this simulation.

Figure (5.5) shows pitch angle distribution functions upstream (thick lines) and downstream (thin lines) for $q = 1$ (solid lines) and $q = 1.5$ (dashed lines). In the downstream region, particles are redistributed in pitch angle be-

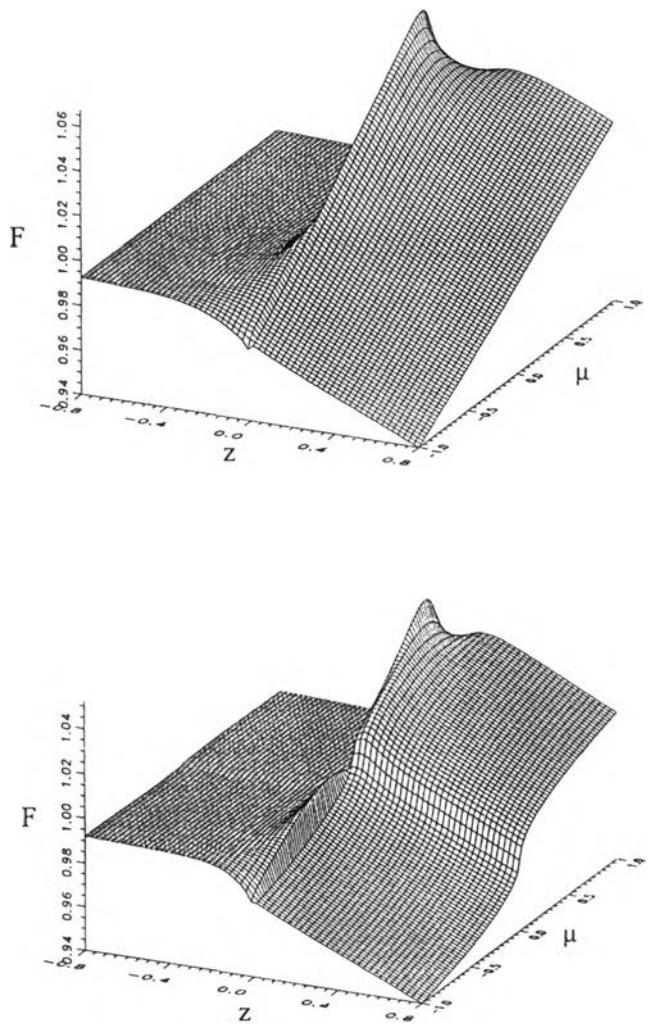

Figure 5.4: Phase space density of particles in the steady state as a function of μ and z (in units of λ) near an oblique, planar shock with $\tan\theta_1 = 4$ for a) $q = 1$ and b) $q = 1.5$. Note the changes in the pitch angle distribution near the shock at $z = 0$.

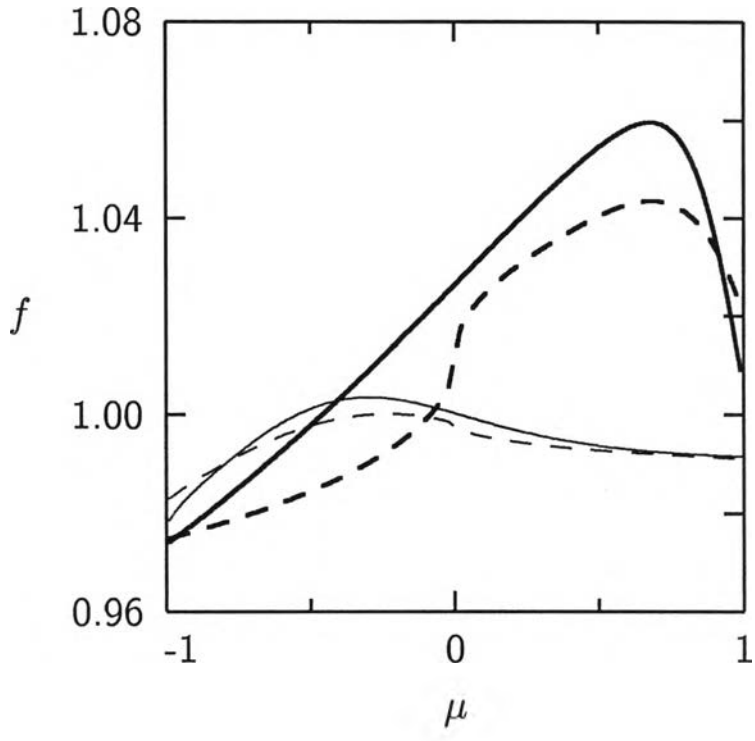

Figure 5.5: Phase space density of particles in the steady state as a function of μ near an oblique, planar shock with $\tan\theta_1 = 4$ for $q = 1$ (solid lines) and $q = 1.5$ (dashed lines) at $z = 0.05\lambda$ (upstream; thick lines) and $z = -0.05\lambda$ (downstream; thin lines).

cause of changes in pitch angle as particles cross the shock; the average flux also increases slightly due to acceleration. It is worth noting that for a highly oblique shock, most particles coming from upstream are in fact reflected, i.e., when $|\mu| < \sqrt{1 - B_1/B_2}$ in the shock frame, or in the case of a strong, highly oblique shock, for pitch angles more than 30° from the magnetic field direction. Another feature of Figures (5.4) and (5.5) is the sharp gradient in f at $\mu = 0$ for the case of $q = 1.5$. For this form of the pitch angle diffusion coefficient, $\varphi(\mu) = A|\mu|^{0.5}(1 - \mu^2)$ tends to zero as $\mu \to 0$. Since the μ-flux, $S_\mu = -(\varphi/2)(\partial F/\partial \mu)$, is slowly varying in a near-equilibrium situation, the vanishing diffusion coefficient at $\mu = 0$ is able to sustain an infinite gradient in F at that value.

The upstream distributions provide another visible manifestation of particle acceleration near the shock. We can see that upstream distributions increase with μ up to $\mu \approx 0.7$. This is because the greatest acceleration occurs for particles reflected with the greatest change in pitch angle (Figure (5.6)).

For the greater μ values, f drops sharply. The reason is that given our assumption of conservation of the magnetic moment, particles with $\mu > \sqrt{1 - B_1/B_2}$, or 0.85 in this case, have come from downstream. A similar drop in f has been called a "deficit cone" (Nagashima *et al.*, 1992) or "loss cone" effect (Bieber and Evenson, 1997) for the case of galactic cosmic ray (GCR) depletion at high μ upstream of an interplanetary shock, which is due to the paucity of GCR coming from downstream. Simulations with this code (Ruffolo, 1999) provided

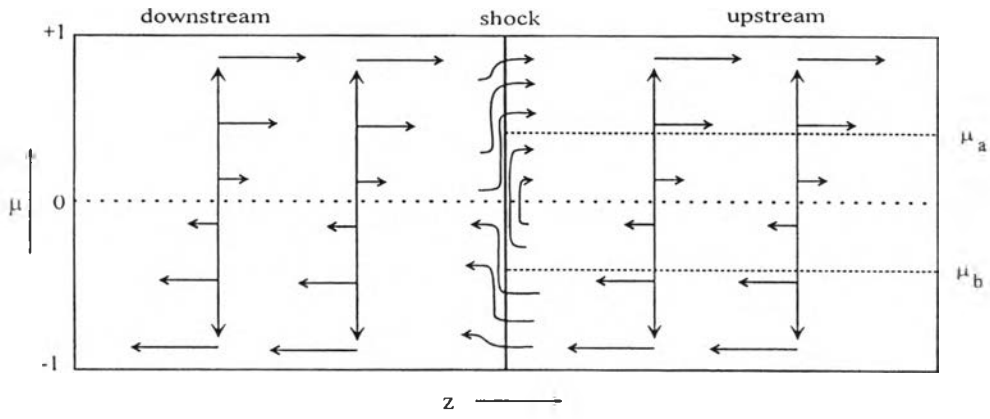

Figure 5.6: Illustration of particle transport near an idealized, oblique shock. The directions of motion of particles in the z-μ plane are indicated by the arrows. Vertical arrows indicate pitch angle scattering, horizontal arrows indicate streaming. and arrows near the shock indicate the changes in μ during transmission or reflection.

the first detailed explanation of this observed effect, which may help to provide advanced warning of space weather effects at Earth (Bieber and Evenson, 1997).

5.2 Steady State Spherical Shock Acceleration

In a steady state, an equilibrium is reached in the evolution of the particle distribution function in terms of position (r), pitch angle (μ), and momentum (p). In practice, the radial distance r is related to the simulation distance z by the relation $z = r - r_{sh}$, where r_{sh} is the shock radius, located at the middle of the simulation length L. By this point of view, $z = 0$ at the shock and $z < 0$ ($z > 0$) is the downstream (upstream) side. In our simulations, we assume that the momentum dependence is given by $F \propto p^{-\delta}$, so we can find the value of δ that yields a steady state for F in terms of z and μ. Figure (5.7) indicates the flux balance that determines δ. Far away from the shock, we can use the diffusive approximation (Ruffolo, 1999) to say that the net z-flux far downstream is dominated by convection, and by this assumption we can set $S_z = u_2 F_0$, where u_2 is the fluid speed in the downstream side and $F_0 = \langle F \rangle_\mu$, the average distribution function over μ at the boundary (the first spatial z cell in the simulation). This boundary condition is not designed for a spherical geometry, but it should be applicable to a good approximation when $L << r_{sh}$. Far upstream we approximate that there is a balance between convection toward the shock and diffusion away, so that $S_z = u_1 F_u$, where F_u is the far upstream distribution of F. In practice

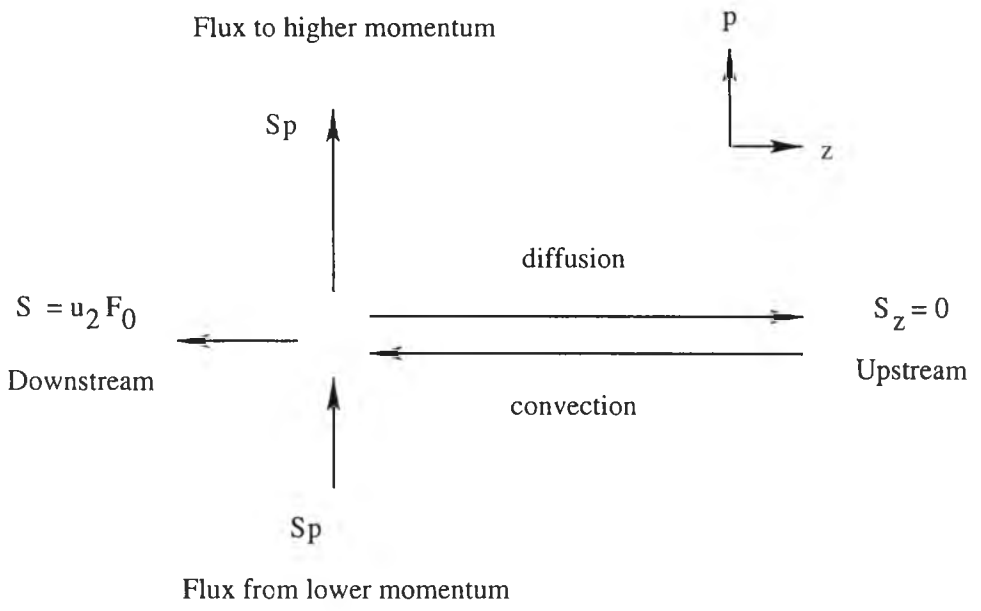

Figure 5.7: Schematic diagram shown the balance of spatial and momentum fluxes in diffusive shock acceleration (Ruffolo, 1999).

we set this value to be zero; hence, there is only a net outflow of particles from the shock in the downstream direction. This is balanced by the p flux, S_p, due to acceleration from the lower momenta to the momentum of interest, as well as from the momentum of interest to the upper momenta, for the appropriate steady state power-law index, δ. In practice, we do not exactly know what the appropriate δ is, so we first estimate a possible δ value and then perform the simulation. By using visualization tools (in this case the IDL package), one can monitor the behavior of the particles in our simulation space as well.

We present results in terms of the intensity $j = F/2\pi r^2$, which is an experimentally measured quantity and is approximately conserved as particles

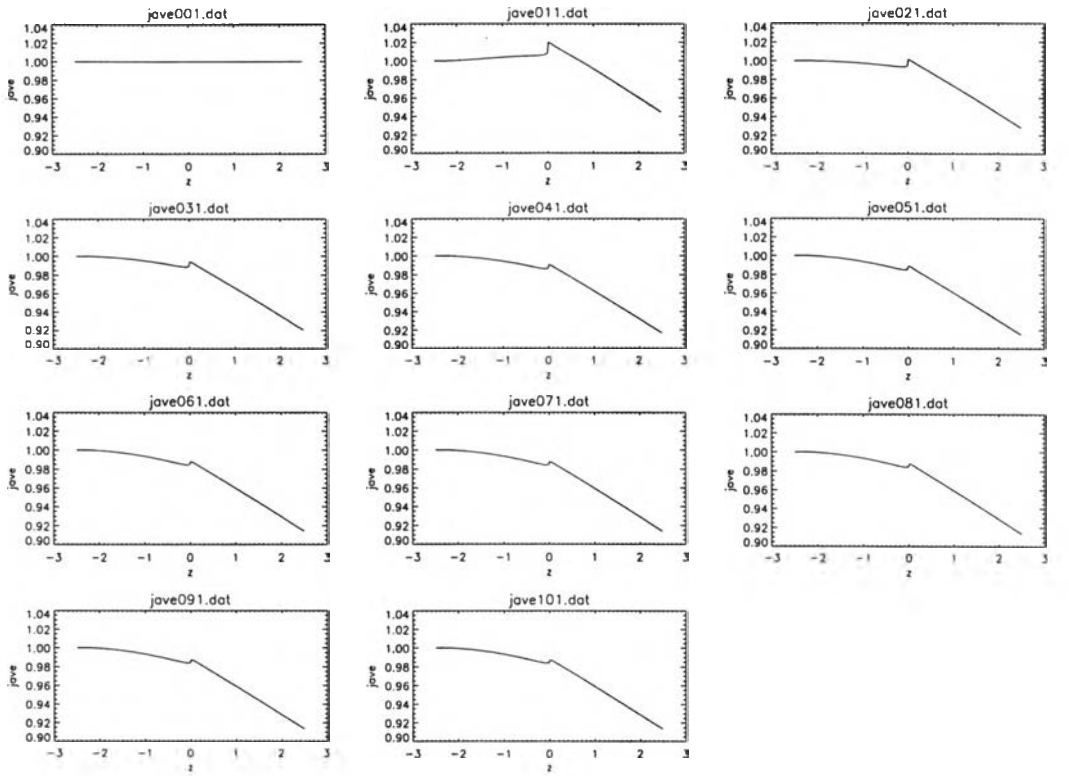

Figure 5.8: The time evolution of j_{ave} vs. spatial distance z for $\delta = 1$. Each frame represents a time interval of 1039.9375 min.

cross the shock.

Figure (5.8) shows an example of a bad δ value (where we set $\delta = 1.0$). From the figure we can see the time evolution snapshots from left to right and top to bottom; the first figure shows the initial condition. The charged particle intensity is averaged over μ: j_{ave} for each spatial grid point tends to decrease while at the beginning it is set to 1 everywhere. Note that the normalization is to $j_{ave} = 1$ at the leftmost (downstream) boundary. The test tells us that the total intensity in the simulation region decreases with time, and one can interpret that the spectral index value is not high enough for the appropriate balance as

in Figure (5.8). In this way the spectral index was adjusted again and again (as estimated by means of linear interpolation) until a steady flux is achieved in the simulation.

Before the real oblique shock simulation was performed, we also tested our methodology for the case of a parallel shock ($\theta_1 = \theta_2 = 0$; θ is the angle between a magnetic field line and the shock normal and 1 (2) indicates the upstream (downstream) side) to reproduce results of Ruffolo (1999). In that case our simulation could reproduce the same results for the same parameters, since our transport equation can be reduced to the same equation as used in that circumstance.

For the oblique case, we consider the *strong* shock case where the compression ratio $r_c = 4.0$ and the relation between θ_1, θ_2, and the fluid speeds upstream and downstream is set as follows:

$$\frac{u_1}{u_2} = \frac{\tan\theta_2}{\tan\theta_1} = 4, \tag{5.1}$$

where u is the fluid speed. By this relation we use $u_1 = 1600$ km/s, corresponding to $u_2 = 400$ km/s on the downstream side. The incident magnetic field $\theta_1 = 75°$ corresponds to $\theta_2 = 86.16°$ on the compressed downstream side. Note that in the solar ecliptic plane under a realistic Archimedean spiral magnetic field configuration this event is occurs at a distance 15.8 AU, where this parameter was directly calculated from the equation

$$\tan\theta = \frac{r_{sh}\Omega}{u}, \tag{5.2}$$

where $\Omega = 2.52 \times 10^{-6}$ radian s^{-1} is the solar rotation rate. We considered protons with speeds v corresponding to a momentum of 499.61 MeV/c. We used a grid spacing of $\Delta z/\lambda = 0.02$ and $\Delta\mu = 2/15$. For convenience, we set $v\Delta t = \Delta z$ and $\Delta t = 0.415975$ min (simulation time). Our simulation length $L = 5.0$ AU; hence, the outer boundaries were placed at $z = \pm 2.5\lambda$.

Figures (5.9-5.10) are the time evolution plots of j_{ave} against the spatial distance, z, from the initial condition to a nearly steady state, where we set $q = 1.0$. According to Chapter 2, q controls the form of the scattering coefficient: $q = 1$ is for isotropic scattering and $q = 1.5$ is in the range of 1.3 to 1.7 inferred by Bieber *et al.* (1986) for actual interplanetary scattering. For the first simulation, we neglected the effects of adiabatic deceleration and set $\delta = 2.0$. Figure (5.10) is an overlay plot of j_{ave} vs. z showing the approach to a steady state in the time evolution where the final time reached is 1039.9375 min. Figure (5.11) is a surface plot of $j(z, \mu)$ for our momentum of interest at the final stage of the simulation. We will clearly see that near the shock boundary the particle intensity jumps suddenly and decays toward zero far upstream. As mentioned earlier, j_{ave} was normalized to 1 at the leftmost (downstream) boundary. We see that j_{ave} is nearly constant and approaches unity at the boundary.

In the next step, we take the effect of adiabatic deceleration into account by using the same parameters as previously. Figures (5.12- 5.14) are plotted in the same manner as Figure (5.9 - 5.11) for comparison.

For the more realistic situation occurring in our solar system (the only

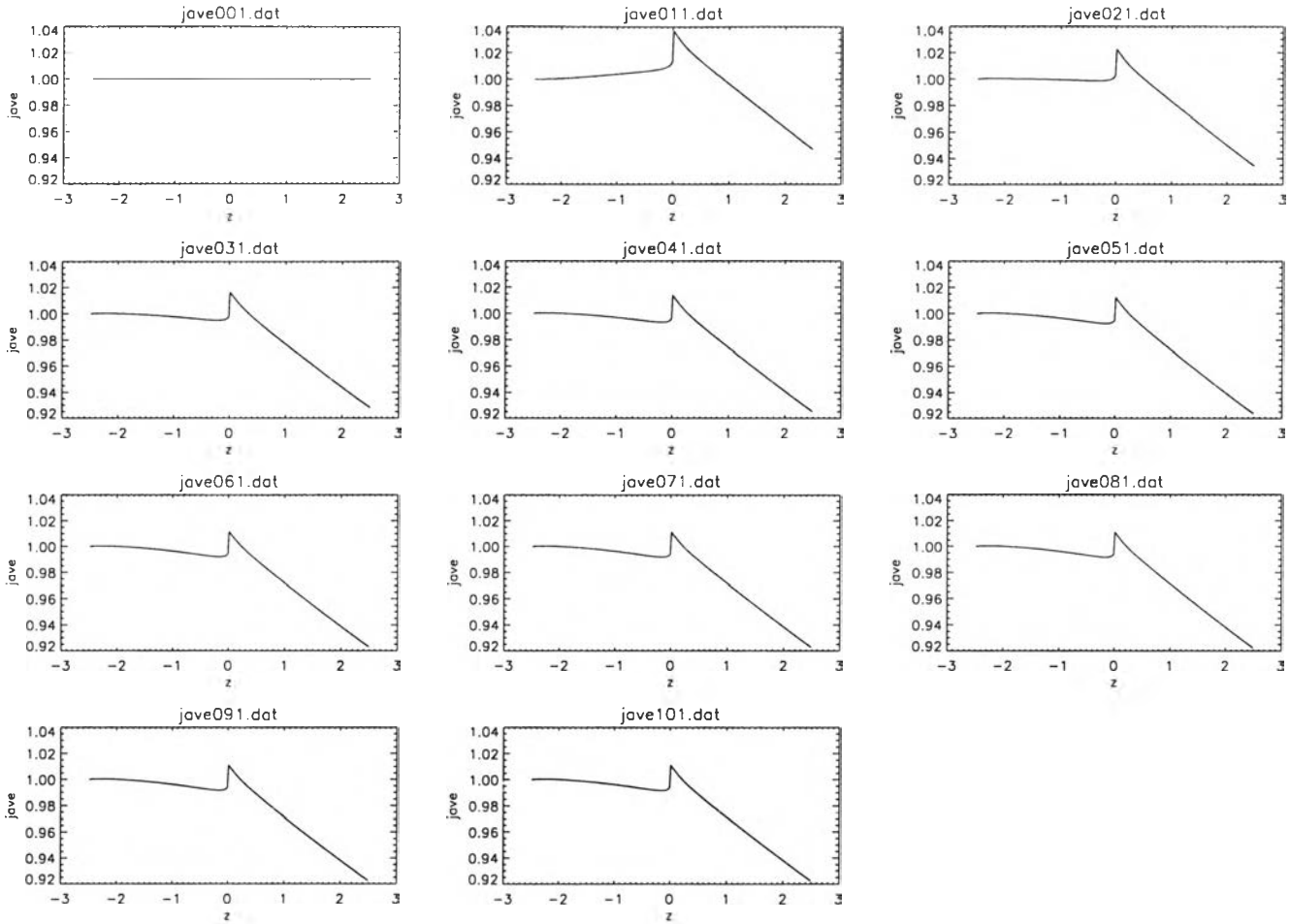

Figure 5.9: The time evolution of the spatial dependence of the pitch angle-averaged intensity, j_{ave} vs. spatial distance z for $q = 1$. The particle intensity in our flux tube is first set equal to a constant at the beginning of the simulation.

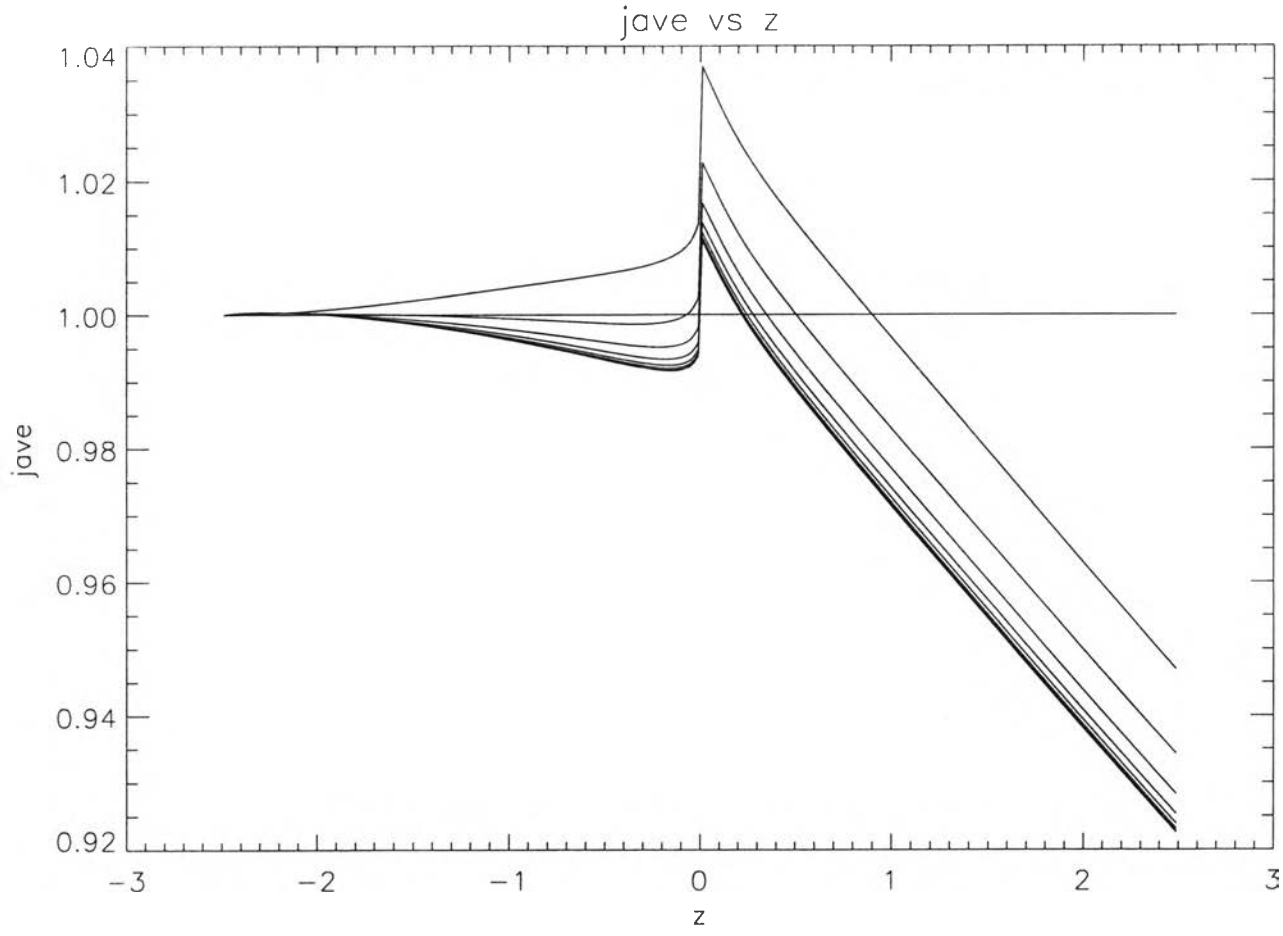

Figure 5.10: Overlay plot of j_{ave} vs. spatial distance z corresponding to the previous plot for $q = 1$. The deceleration effect is not taken into account. These line plots illustrate the approach to a *steady state*.

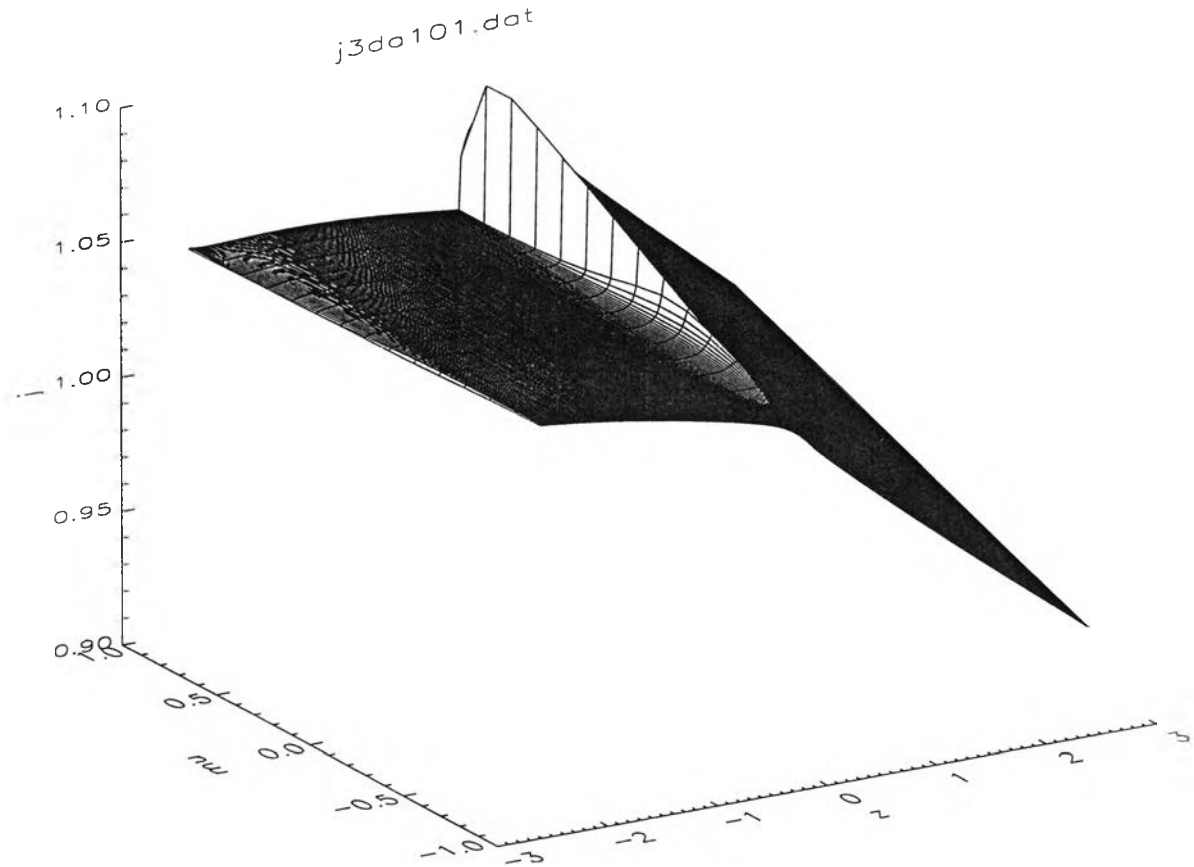

Figure 5.11: Surface plot showing the distribution of the particle density j in $\mu - z$ space for $q = 1.0$ and no adiabatic deceleration effect.

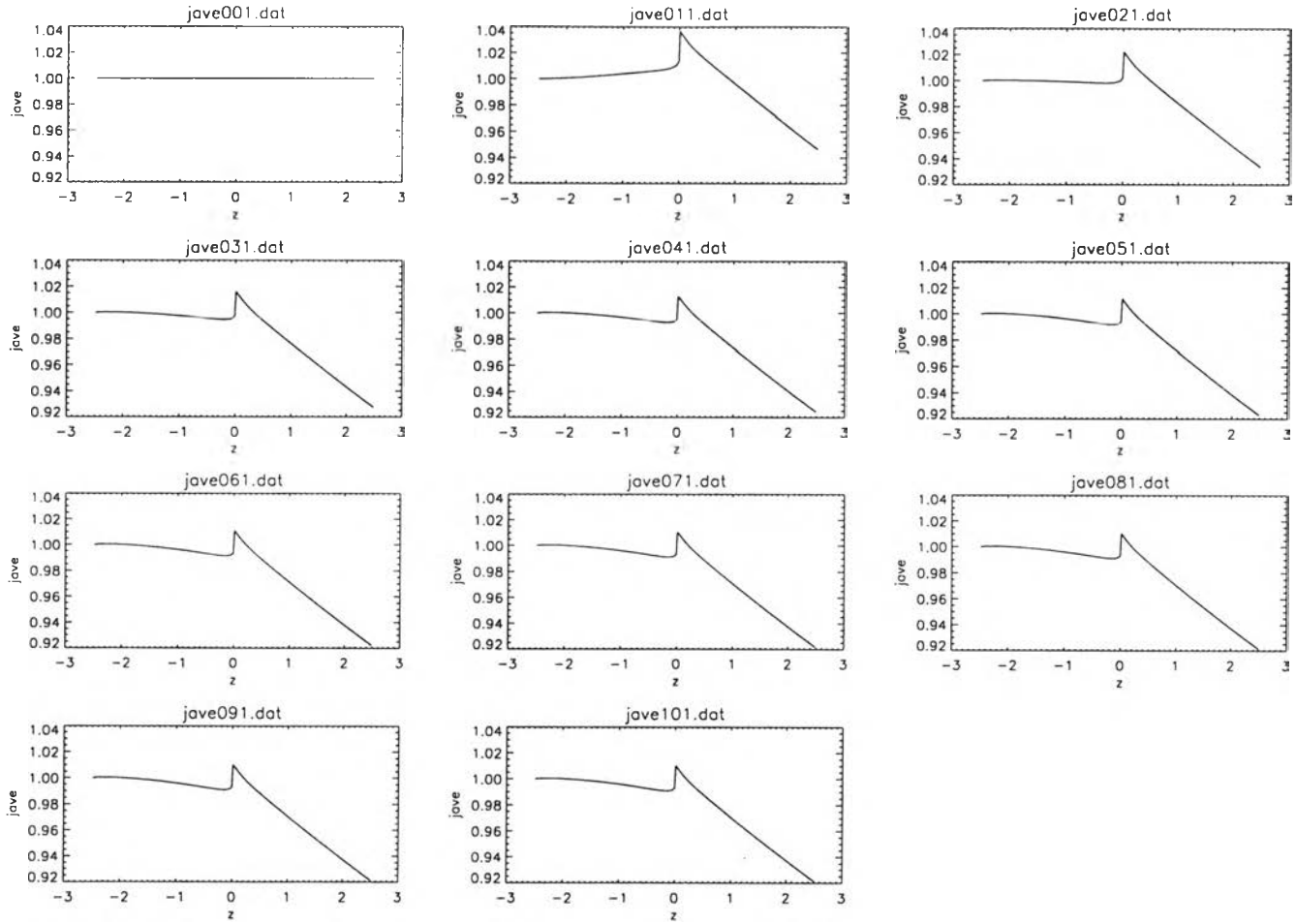

Figure 5.12: Same as Figure (5.9) but including the adiabatic deceleration.

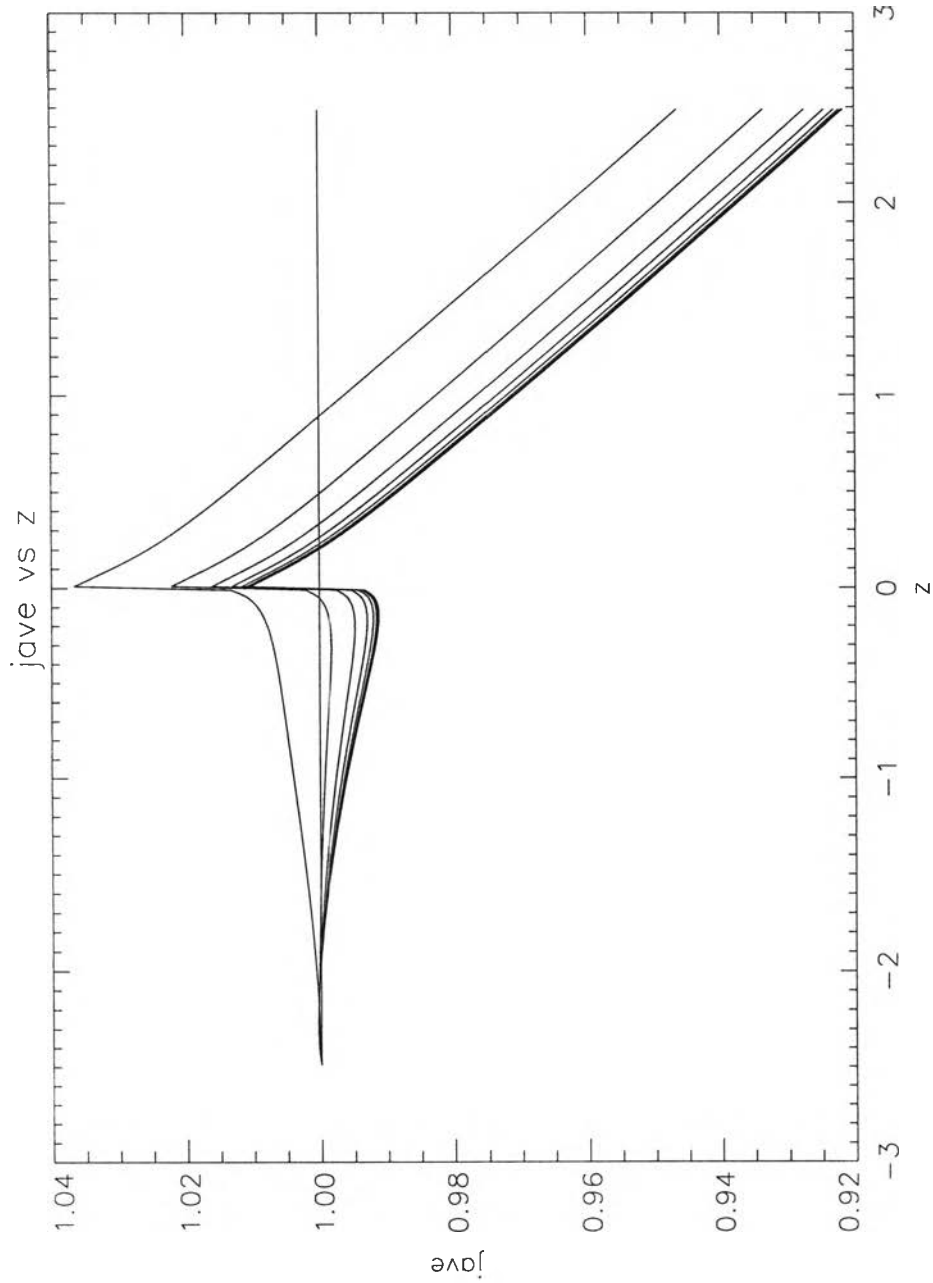

Figure 5.13: Same as Figure (5.10) but including the adiabatic deceleration.

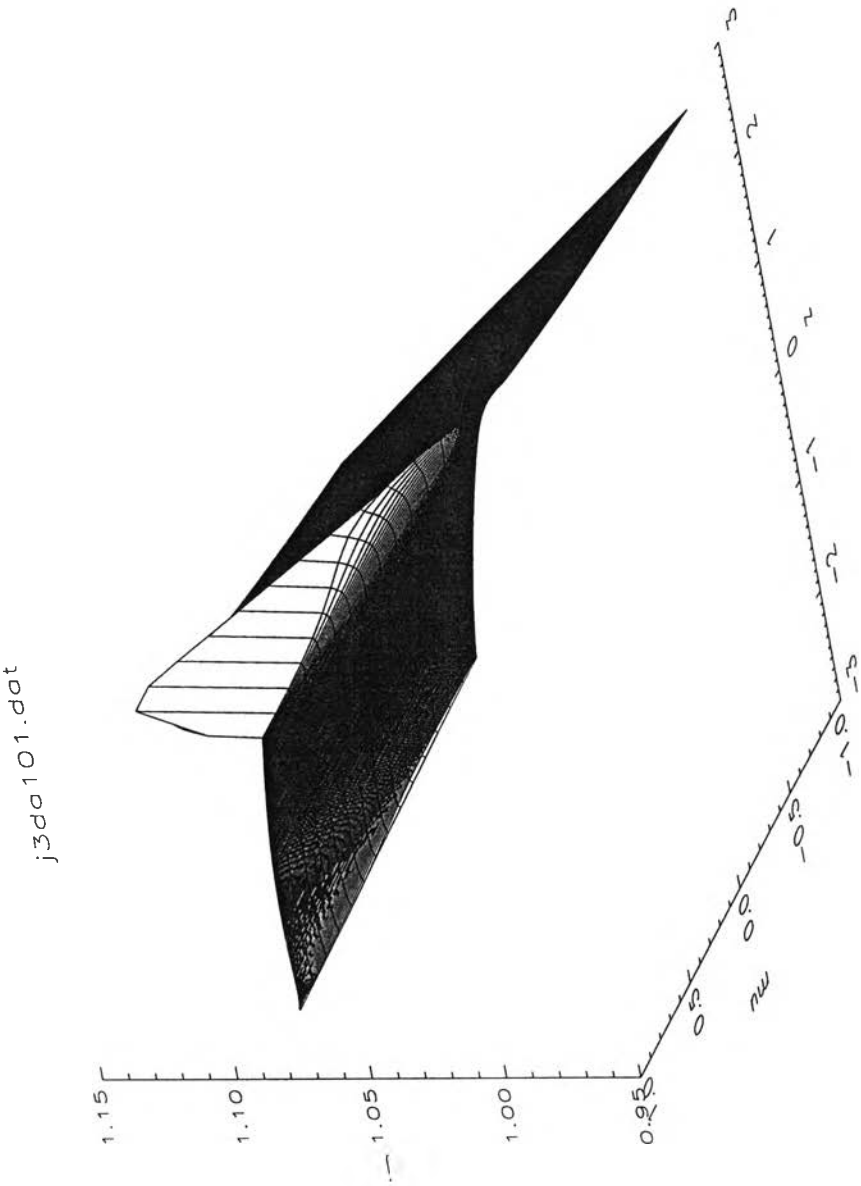

Figure 5.14: Same as Figure (5.11) but including the adiabatic deceleration.

place where cosmic ray acceleration can be studied *in situ*), we now set $q = 1.5$, as appropriate for the interplanetary magnetic field (IMF). Other parameters were the same. Figures (5.15 - 5.17) neglected the effect of adiabatic deceleration while Figures (5.18 - 5.20) considered this effect again.

Figure (5.21) compares the spatial dependence of the pitch angle-averaged particle density, $\langle j \rangle_\mu$, for steady state particle acceleration near a shock (at $z = 0$) for $q = 1.0$ with no effect of deceleration (solid line) and when the adiabatic effect is included (dashed line). For $q = 1.5$, we plot the two lower lines, the upper one obtained when no deceleration effect is taken into account.

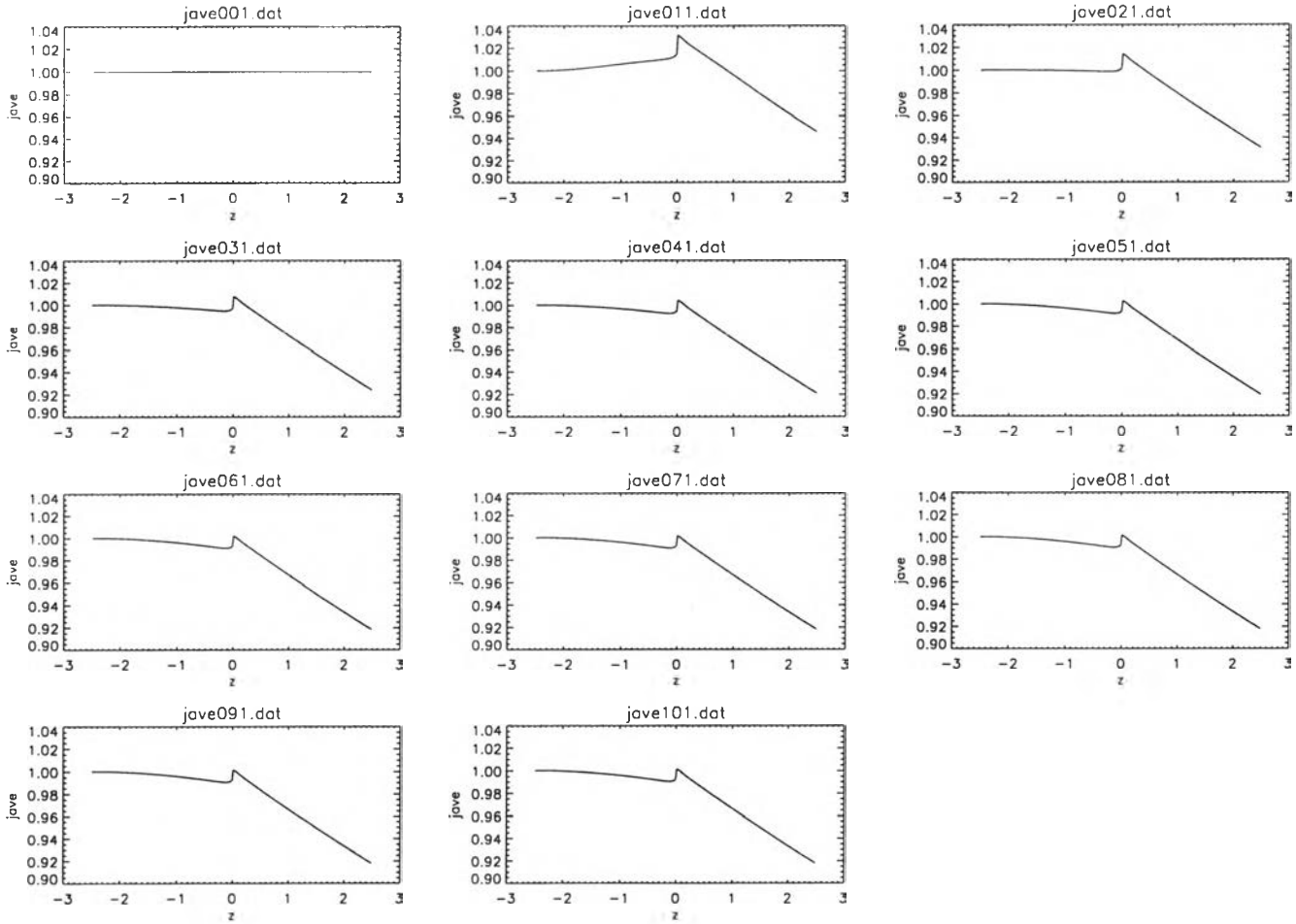

Figure 5.15: Like Figure (5.9) for $q = 1.5$ and no deceleration effect.

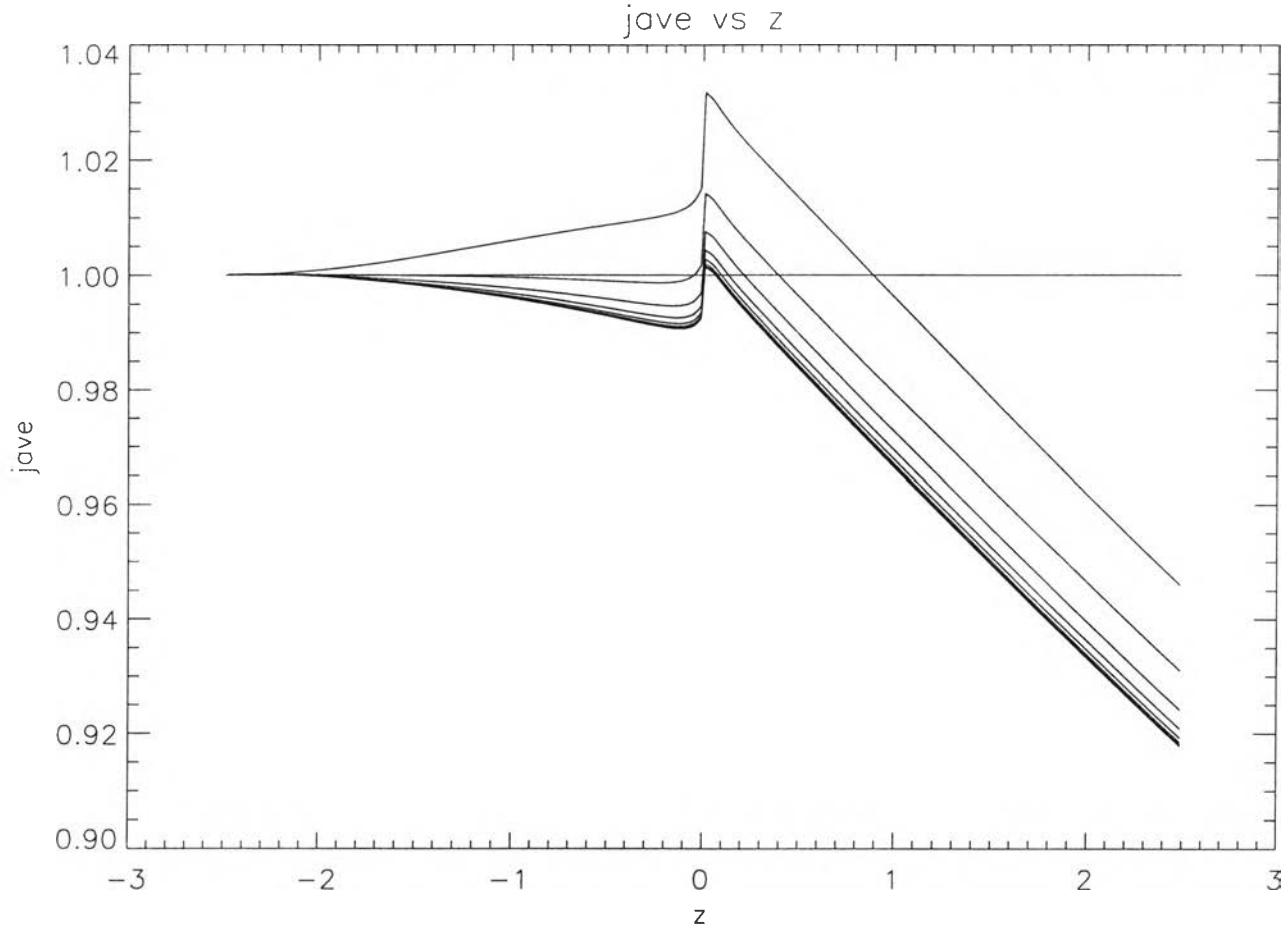

Figure 5.16: Like Figure (5.10) for $q = 1.5$ and no deceleration effect.

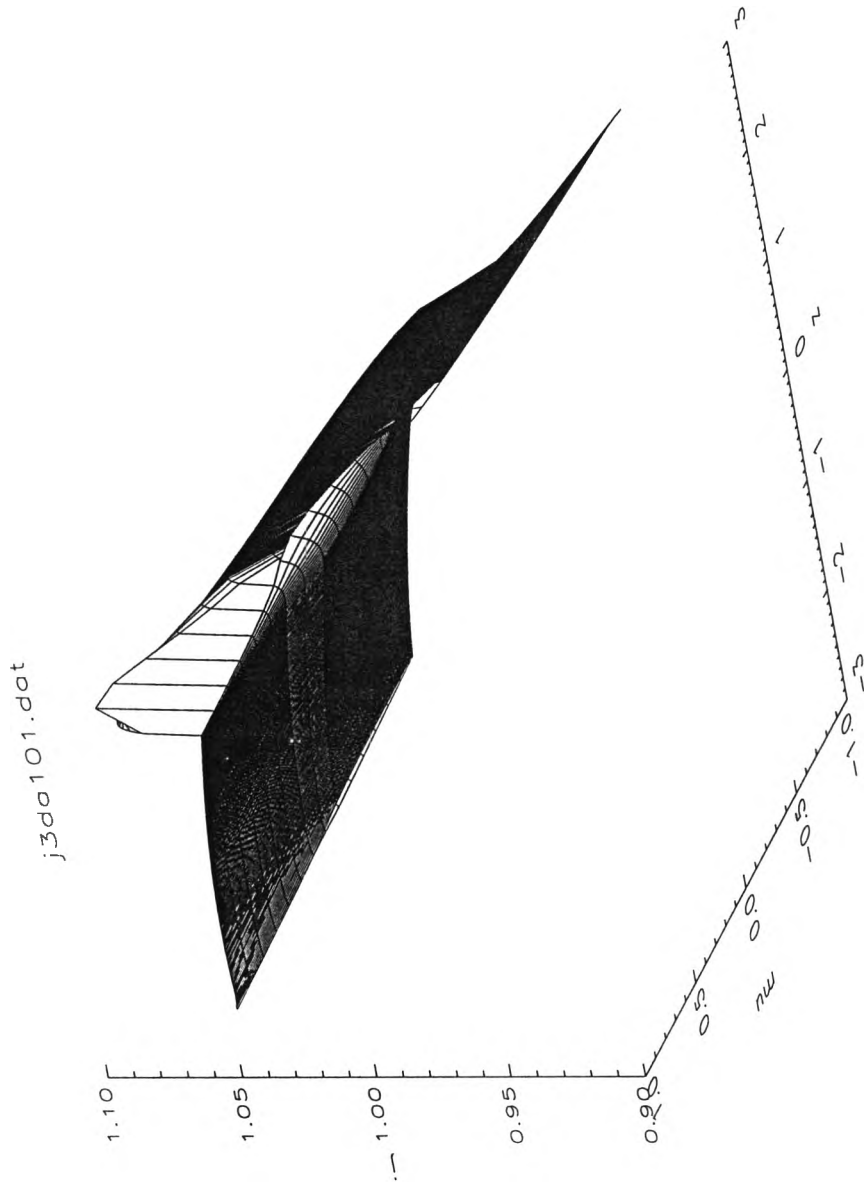

Figure 5.17: Like Figure (5.11) for $q = 1.5$ and no deceleration effect.

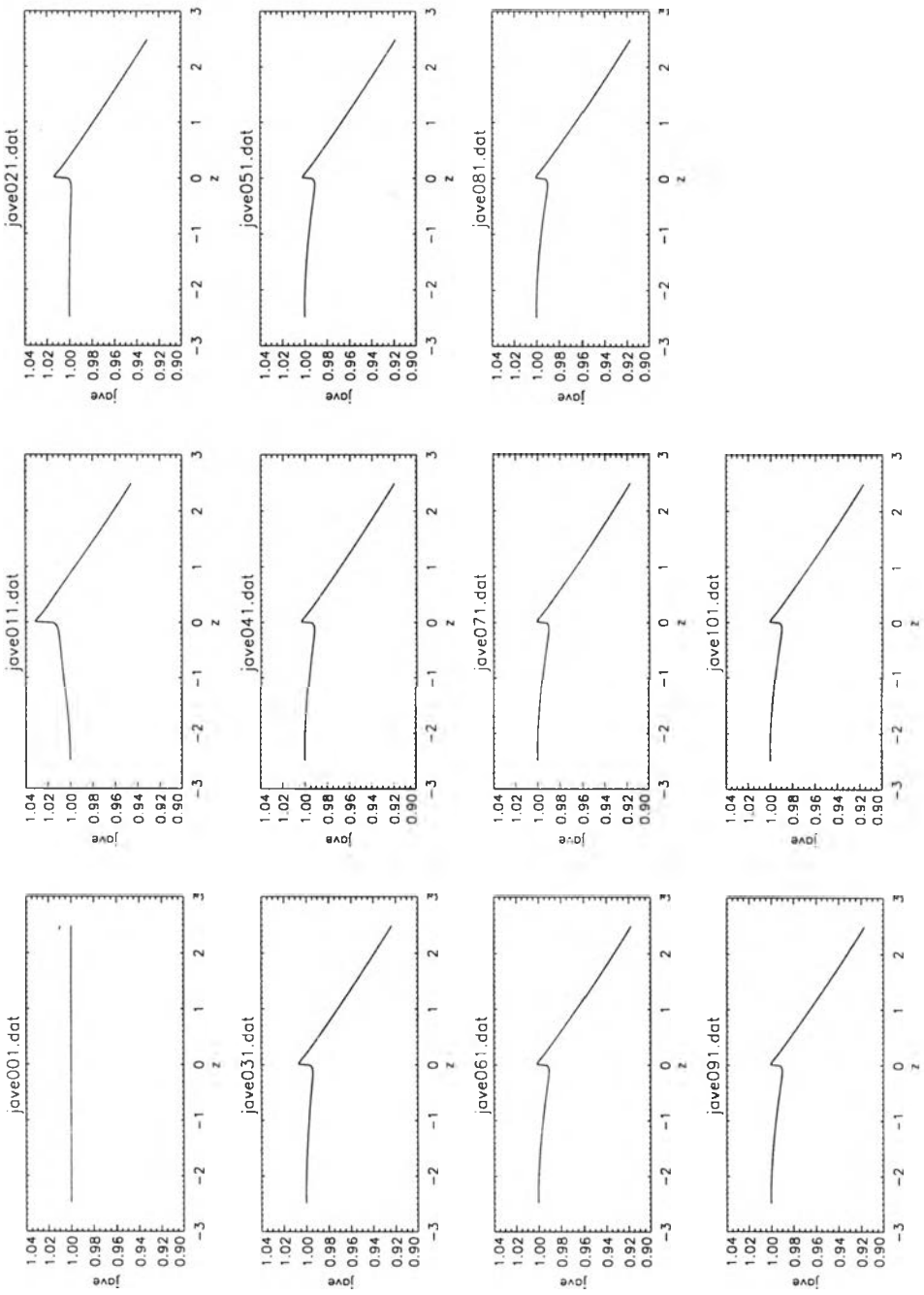

Figure 5.18: Like Figure (5.12) for $q = 1.5$ and including the effect of deceleration.

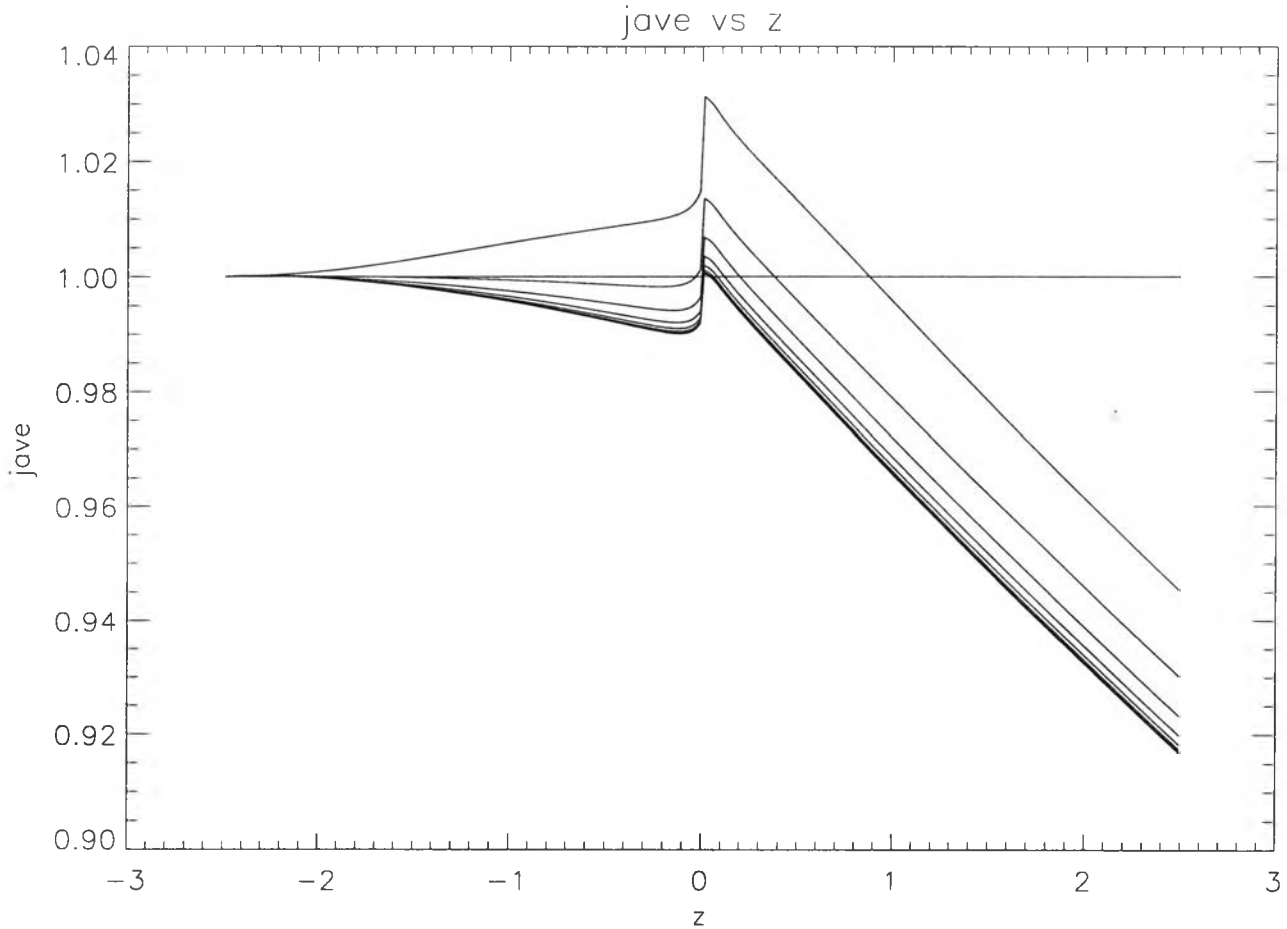

Figure 5.19: Like Figure (5.13) for $q = 1.5$ and including the deceleration effect.

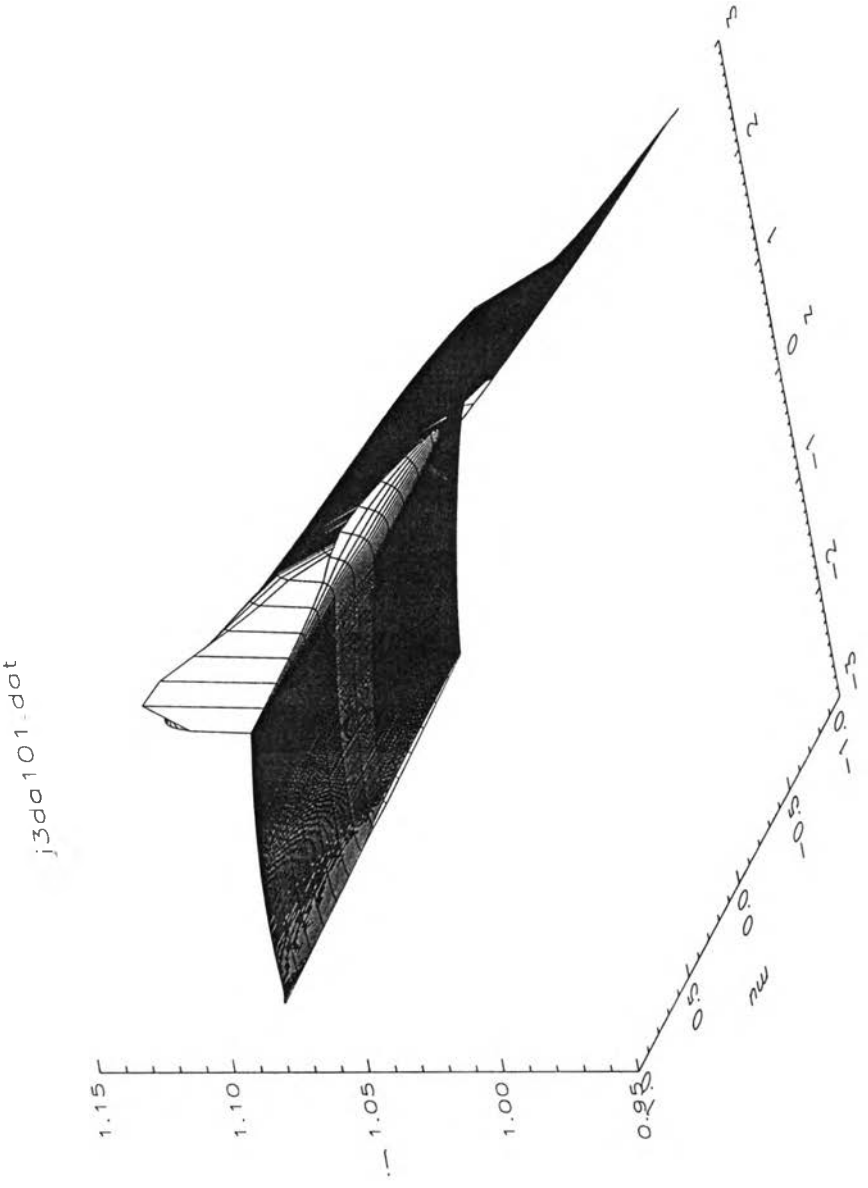

Figure 5.20: Like Figure (5.17) for $q = 1.5$ and taking the effect of adiabatic deceleration into account.

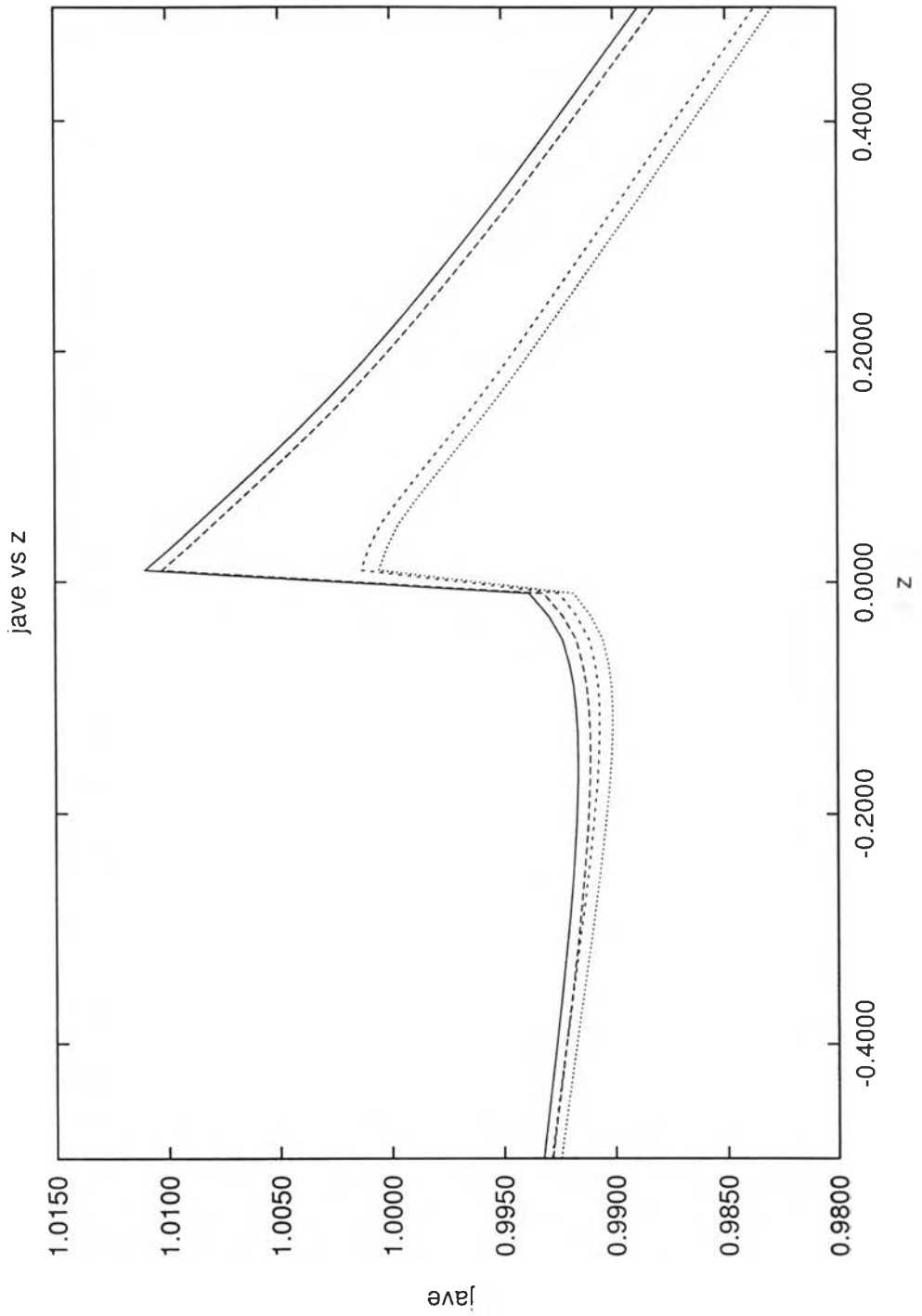

Figure 5.21: Graphs of $\langle j \rangle$ vs. z for $q = 1$ (upper group) and $q = 1.5$ (lower group) where within each group the higher curve is for neglecting the adiabatic deceleration effect and the lower curve is for including it.